Research Article

Received: 6 August 2018 Revised: 19 September 2018 Accepted article published: 30 September 2018 Published online in Wiley Online Library: 12 November 2018

(wileyonlinelibrary.com) DOI 10.1002/pi.5713

Fast scanning calorimetry clarifies the understanding of the complex melting and crystallization behavior of polyesteramide multi-block copolymers

Ashwinikumar Sharma,[a,b] Guilhem P Baeza,[c] Luna Imperiali,[b] Wilco PJ Appel,[b] Carel Fitié,[d] Geert Vanden Poel[d] and Evelyne van Ruymbeke[a*]

Abstract

Fast scanning calorimetry has been applied in order to understand the phase transitions in thermoplastic elastomers (TPEs) based on well-defined multi-block copolymers made of 'soft' polytetrahydrofuran and 'hard' terephthalate ester diamides. The intrinsically complex chemical structure of TPEs leads to complex phase transitions. By changing their thermal history over a wide range of temperature (from −100 °C to 200 °C) and cooling rates (from 10 to 4000 °C s^{-1}), we clarify the origins of the various phases present in these materials. In particular, we study the different possibilities for the hard segments to associate depending on their mobility during the quenching phase, forming either strong and stable structures or weaker and metastable ones. Besides, we demonstrate that a minimal cooling rate of 800 °C s^{-1} is necessary to keep these TPEs (made of short and monodisperse hard segments) amorphous leading to a subsequent cold crystallization when heating back, at around 30 °C. Finally, we validate our interpretations by varying the copolymer composition (from 10 wt% to 20 wt% hard segments), revealing the thermal invariance of poorly organized domains. Based on these data, we also discuss the importance of chain diffusion in the crystallization process. Applying fast scanning calorimetry allows us to link fundamental understanding to industrial application.

Supporting information may be found in the online version of this article.

Keywords: multi-block copolymers; polymer crystallization; fast scanning calorimetry; thermoplastic elastomer

INTRODUCTION

Thermoplastic elastomers (TPEs) form an industrially relevant class of materials due to their tunable engineering properties and they find numerous applications in the automotive, consumer electronics as well as household appliance sectors.[1] The philosophy behind these elastomers resides in the phase separation of block copolymer into hard and soft domains providing good mechanical properties and elasticity combined with ease of processing.[2,3] The hard domains are either amorphous, high-T_g[4,5] or crystalline,[6,7] made of aggregated 'hard' segments (HSs) playing the role of physical crosslinks whilst the soft domains encompass low-T_g 'soft' segments (SSs) such as polybutadiene,[4] polypropylene oxide[8] or polytetrahydrofuran[9] (pTHF). In industrial applications, the SS molecular weight is most often a few kilograms per mole, probably limiting their crystallization.[10] On the other hand, the crystallization behavior of the HSs is governed by their distribution along the chain, as well as by the molecular weight of the SSs and of the whole chain.

The strong asset of TPEs consists in their behaving as rubbers at room temperature while being melt-processable above their order–disorder transition temperature. This dual behavior makes them important candidates to replace vulcanized elastomers in a wide variety of consumer goods, notably from a recycling or reshaping point of view.[11] Another important advantage lies in the high tunability of their properties by modifying both the composition and the chemical architecture[12] of the copolymers, particularly by using HSs interacting through supramolecular bonds enhancing their phase separation. Recently the utilization of, for example, urea,[13] urethanes[5,14] or amide groups[9,15] as HSs has been reported, leading in the latter case to ribbon-like crystallites observable through microscopy[14,16] and/or scattering techniques,[17,18] providing materials with strong mechanical properties.[19]

* *Correspondence to: E van Ruymbeke, Bio and Soft Matter, Institute of Condensed Matter and Nanoscience, Université catholique de Louvain, Louvain-la-Neuve, Belgium. E-mail: evelyne.vanruymbeke@uclouvain.be*

a *Bio and Soft Matter, Institute of Condensed Matter and Nanoscience, Université catholique de Louvain, Louvain-la-Neuve, Belgium*

b *DSM Material Science Center, Geleen, The Netherlands*

c *University of Lyon, INSA-Lyon, CNRS, MATEIS, Villeurbanne, France*

d *DSM Engineering Plastics B.V., Geleen, The Netherlands*

Among the various classes of TPEs such as styrene based or olefin based, polyesteramides present assets from both polyesters and polyamides such as high melting temperature, fast crystallization and good mechanical properties. Moreover they consist of one T_g and one main T_m with values in between the T_g and T_m of polyesters and polyamides, showing a T_g/T_m ratio of 0.65, as HSs separate by crystallization.[15] Such multi-block polyesteramides are usually prepared through a two-step synthesis. First, well-defined HS units (terephthalate ester diamides, bisesterdiamides, T4T) are synthesized from 1,4-butane diamine and dimethyl terephthalate, further purified by recrystallization.[20] Then, HS units are connected with SSs via condensation polymerization in order to form multi-block copolymers.[2,15,21] Of great importance, Gaymans and co-workers reported a strong dependence of both thermal and mechanical properties on the length and polydispersity of the HSs they contain. In particular, based on experimental techniques such as DSC, Fourier transform IR, dynamic mechanical thermal analysis and tensile set measurements, they demonstrated that small and monodisperse hard units were providing faster crystallization, higher elasticity (with minor temperature dependence) and higher fracture strain.[19,21]

Recently, we studied the multi-scale structure of one of these TPEs consisting of a sequence of pTHF and terephthalate based diamide T4T segments with varying HS content from 5 to 20 wt%.[17] At a local length scale, we reported the different ways for the HSs to stack, i.e. either by directive hydrogen bonding or by van der Waals interactions with possible $\pi-\pi$ stacking. While the former is responsible for the fast growth along a preferential direction, and thus for the elongated (ribbon-like) nature of the aggregates, the latter allows the crystallites to widen perpendicularly (the thickness being fixed by the HS dimension, *ca* 2.1 nm).[17] Also, by showing quite broad endothermic peaks, conventional DSC suggested that these hot-pressed materials were made of a wide molecular weight distribution of hard domains similarly to other TPEs based on polybutylene terephthalate (PBT) or polyamide 6,6.[22,23] In contrast, their solvent cast counterparts were characterized by sharp transitions at high temperature, i.e. an enhanced order, probably due to higher chain mobility during the drying phase.

Besides, we observed a low degree of undercooling ($\Delta T_m = T_m - T_c \approx 20 \pm 4\,°C$) for these samples (containing 5, 10, 15 and 20 wt% HSs) due to enhanced HS order, in comparison to PBT based TPEs ($\Delta T_m \approx 36\,°C$).[15,24] Beyond the faster kinetics of aggregation provided by the hydrogen bonds, these low ΔT values suggest a pre-existing order in the melt state probably coming from persistent interactions at high temperatures. In fact, while no phase separation or particular order was detected with classic polarized light microscopy,[25] small angle X-ray scattering resolved in time and temperature revealed unambiguously the presence of HS persistent aggregates at $T > T_m$.[17]

To sum up, it appears that most of the final properties of semicrystalline TPEs depend strongly on a large variety of parameters starting from the chemical nature of the chain segments, their phase separation kinetics and their underlying microstructure. While the chemical composition is crucial, it does not completely set the final behavior of a product: the processing conditions have to be taken into consideration. For instance, industrial techniques/manufacturing processes, such as plastic molding, blow molding, fiber spinning or 3D printing in which crystallization must occur quickly to reduce cycle times and therefore enhance production rate, are likely to lead to unique microstructures due to the very particular temperature gradient and high mechanical stress applied to the materials.[26] The objective of the present work was to apply fast scanning calorimetry (FSC) in order to investigate the crystallization behavior of polyesteramides up to extreme conditions, i.e. varying the cooling rate from 10 to 4000 °C s^{-1}. Our results evidence the latter's effect on the TPE mesoscopic structure, providing new insights for control of the mechanical properties.

In addition, we discuss the role of isothermal time, temperature and chain mobility on the formation of the crystallites (either stable T4T ribbon or metastable 'baby-ribbon') and study their consequences on the sample properties. As a more general objective, we show the importance of understanding the crystallization behavior in order to improve industrial application.

The paper is organized as follows. The sample preparation for FSC and the related methods used for the different experiments are presented next. In the following section, we present and discuss the thermograms obtained during the heating phase (the so-called 'measurement') by varying (i) the cooling rate from the melt state prior to the measurement, (ii) the cooling path, i.e. comparing single ramp with two-step quenching, (iii) the isothermal crystallization temperature (T_{iso}) at which the sample is set prior to the measurement and (iv) the corresponding time t_{iso} spent at a given T_{iso}. The last part (v) is dedicated to the impact of the chain composition by varying the HS content from 10% to 20%. We then use these different results to discuss and interpret the bimodal distribution found for the crystallization rate as a function of the isothermal crystallization temperature at a high density of HSs. Conclusions are drawn in the final section.

MATERIALS AND METHODS

Materials

Well-defined linear TPEs (multi-block copolymers) containing 5, 10, 15 and 20 wt% HSs were synthesized via polycondensation of pTHF and T4T ester diamides (T, terephthalate; 4 is the number of carbon atoms between the two consecutive T groups). The molecular weight was extracted through exclusion size chromatography in hexafluoroisopropanol and gave $\overline{M_n} \approx 25\,kg\,mol^{-1}$ with a polydispersity of 2. The HSs are monodisperse and made of a T4T-diamide group whereas the SS chain length shortens with increasing HS content. Quantitative details on the chain structure and additional information on the synthesis can be found in supporting information, Section A.1, A.2 and Fig. S1 and in our previous study.[17]

Instrumentation and sample preparation

Conventional DSC

DSC thermograms were recorded on a Mettler Toledo DSC821e from Switzerland equipped with STARe software. Calibration was performed using three standards, covering the wide temperature range required for measuring the TPEs (−100 to 300 °C). The polymer samples were dried overnight in a vacuum oven at 60 °C and subsequently measured at 10 °C min^{-1}, both for cooling and heating. The melting (T_m) and crystallization (T_c) temperatures were respectively extracted from the second heating and first cooling steps. The degree of crystallinity was calculated from the experimental melting enthalpy normalized to the corresponding value for the neat T4T (see Table 1). Note that the thermograms (second heating step) were reshaped by means of baseline correction.

Fast scanning calorimetry (FSC)

Fast scan measurements were performed by using a commercially available fast scanning calorimeter from Mettler Toledo,

Table 1. Physicochemical characterization for all four TPE samples based on SEC and DSC

HS (wt%)	M_n (g mol^{-1})	M_w (g mol^{-1})	ΔT^a (°C)	T_g (°C)	T_c (°C)	T_m (°C)	$X_c{}^b$ (wt%)
5	25 200	48 900	19.2	−60.0	72.8	92.0	2.6
10	22 800	44 300	18.8	−59.1	103.8	122.6	6.3
15	22 500	43 300	20.9	−59.2	125.5	146.4	9.3
20	19 300	37 600	19.2	−59.5	139.2	158.4	15.8

[a] $\Delta T = T_m - T_c$.
[b] Mass fraction of T4T crystallites: X_c (%) = $(\Delta H_{DSC}/\Delta H_{T4T^*})100$ where $\Delta H_{T4T^*} = 150$ J g^{-1} from reference 17.

Switzerland, with a Huber TC100 intercooler and nitrogen purge gas at 50 mL min^{-1}. A detailed description of instrumentation, operating procedure and calibration is given in the literature.[27–31] The performance of FSC depicts the actual high cooling and heating rates as a function of the purge gas and flow rate studied by Vanden Poel *et al.*[29] shows how the applied high heating and cooling rates can be achieved, over a temperature range based on type and flow rate of purge gas used. The calorimetric chip-sensor was conditioned three times followed by temperature correction/adjustment considering the specific thermal environment. This procedure was performed according to the instrument specification prior to use. The bulk sample was reduced to a small piece (of about 100 ng) and then transferred to the sensor center having a diameter of 0.5 mm.[27] The sample mass of the pTHF-T4T samples was determined based on the method explained in the recent book on FSC by Schick and Mathot,[32] using $m = \Delta H_{FSC}/\Delta h$, where ΔH_{FSC} is the enthalpy of melting measured by using FSC at a typical heating rate (10, 100 or 500 °C s^{-1}) and Δh is the specific enthalpy of melting using conventional DSC at 20 °C min^{-1}. Here, the tiny amount of the samples aims to reduce the thermal inertia ('lag') within the materials drastically, allowing high scanning rate measurements.[29,31] Samples were well preserved from degradation due to the nitrogen atmosphere allowing the same piece of TPE to be measured through successive temperature loops.[33] Additional information can be found in supporting information, Section A.3 and Fig. S2.

Effect of cooling rate. Starting from the melt state (200 °C) for 10 s, the sample was cooled to −80 °C at a rate varying from 10 °C s^{-1} to 4000 °C s^{-1}. After the sample was held for 10 s at −80 °C it was subsequently heated back to 200 °C at a constant heating rate of 1000 °C s^{-1}. The heating rate of 1000 °C s^{-1} was selected based on previous studies by Vanden Poel and colleagues[29] showing that the thermal lag corrections remain relatively low up to this heating rate (a maximum lag of −1.4 °C was observed for a 1 µg sample).[29] The corresponding temperature program is presented in Fig. 1(a).

Isothermal crystallization ($T_m - T_g$). Isothermal crystallization measurements were performed on samples covering the entire temperature range from T_m (Table 1) to T_g (*ca* −60 °C) in order to calculate the crystallization rate. Starting from the melt state (200 °C), the sample was quenched to T_{iso} at a cooling rate of 4000 °C s^{-1} to avoid any crystallization and held at this temperature for a time $t_{tso} = 2$ s, after which the material was further quenched to −80 °C at the same cooling rate. In order to understand the crystallization behavior of the pTHF-T4T material small steps of 5 °C at T_{iso} were performed, from T_m to T_g. After holding for 10 s at −80 °C, the sample was finally heated back to 200 °C at 1000 °C s^{-1} (see Fig. 1(b)). In the following sections, this protocol is referred to as two-step quenching. A similar set of measurements was also performed on increasing t_{iso} to 60 s (see Fig. 1(c)).

Atomic force microscopy (AFM)

The morphology of the 20% HS sample was studied with a Bruker Icon Dimension atomic force microscope in tapping mode using an AR5T-NCHR high aspect ratio tip ($k = 42$ N m^{-1}, $f = 330$ kHz, tip radius 15 nm) commercially obtained from Nanosensors. Silicon wafers with 20 nm of electron-beam-deposited silver were used as substrates. The 20% HS sample was first dissolved in THF at a concentration of 1% by weight and subsequently drop cast (500 µL) on the substrate before being dried overnight in a vacuum oven at 65 °C. The resulting film of *ca* 500 nm thickness was then heated to 200 °C under an inert atmosphere and finally either quenched in liquid nitrogen or slowly cooled (6 °C min^{-1}) to room temperature in order to mimic the slow and fast cooling experiments. The uniform surface of the film was scanned for a morphology study of these samples (see supporting information, Section A.4 and Fig. S3).

Rheology measurements (time sweeps)

Dynamic time sweeps were performed in the linear regime with a stress-controlled rheometer (MCR 301 from Anton Paar, Austria) equipped with stainless steel parallel plates of diameter 8 mm (1% strain, 10 rad s^{-1}). All measurements were carried out in a nitrogen gas atmosphere and temperature control was achieved by means of a convection oven (better than ±0.3 °C). Samples were first heated above T_m and then cooled to $T_c + 10$ °C when the storage and loss moduli were measured as a function of time.

RESULTS AND DISCUSSION

The thermal properties of the four TPE samples, containing 5%, 10%, 15% and 20% HSs, were first studied using conventional DSC with a heating rate of 10 °C min^{-1} (see Fig. 2). The thermograms exhibit the glass transition (T_g) of the pTHF SSs at around −60 °C followed by the melting point of the SSs close to −10 °C. The latter is known to occur for SSs having a molecular weight above 2 kg mol^{-1}.[10,17] As expected, the fraction of such SS crystallites decreases with increasing HS content. On the other hand, the melting peak (T_m) of the T4T crystallites follows the HS content well, increasing from 92 °C to 158 °C when the HS density is varied from 5% to 20% HSs. The Fourier transform IR spectra reported in supporting information, Fig. S1(c) also show an increase in absorbance at 1630 cm^{-1}, 1670 cm^{-1} and 3320 cm^{-1} corresponding respectively to the crystalline amide, the amorphous amide and the hydrogen-bonded N–H when the HS content is increased. For the whole sample set, we report in Table 1 the above mentioned parameters as well as the crystallization temperature T_c measured during the cooling step performed at 10 °C min^{-1}.

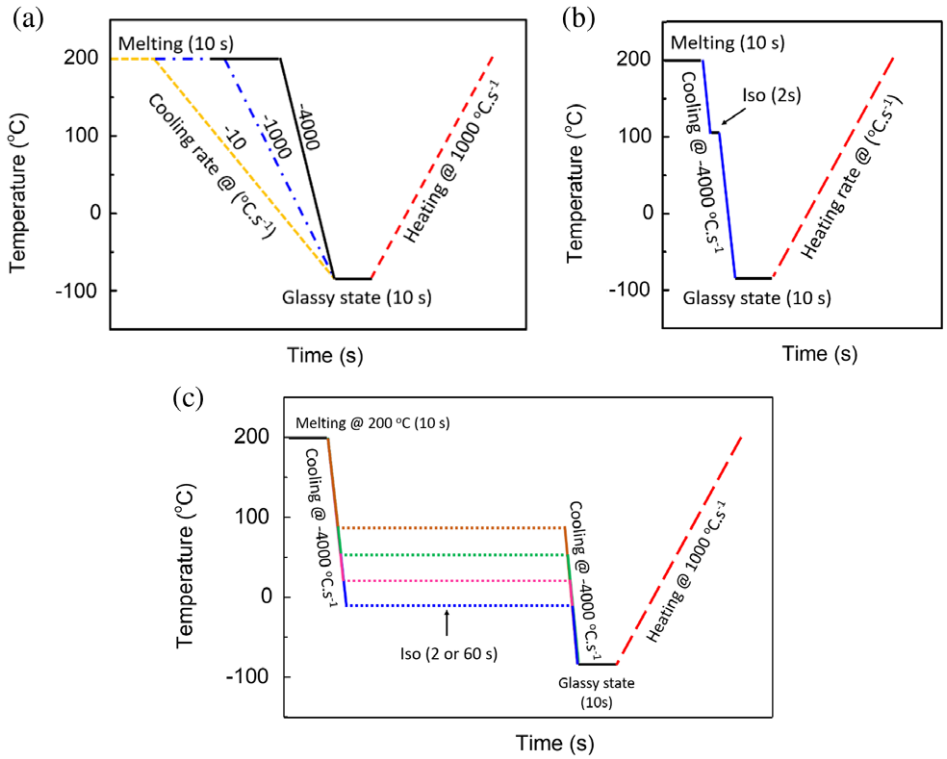

Figure 1. Different thermal treatments used in fast scanning calorimetry in this paper: (a) varying the cooling rate; (b) under isothermal crystallization at T_{iso} = 100 °C, based on a two-step quenching protocol; (c) varying the temperature T_{iso} at which the sample is kept 2 s before the measurement as well as the waiting time at T_{iso}.

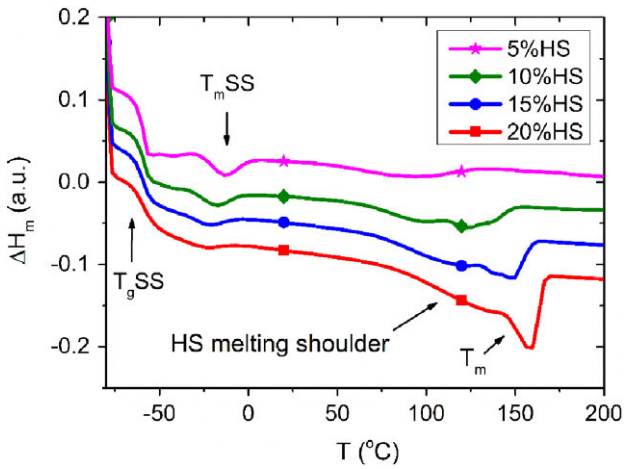

Figure 2. DSC thermograms of TPEs containing 5%, 10%, 15% and 20% HSs performed at a heating rate of 10 °C min^{-1}. Data have been vertically shifted for clarity. Respective values of T_g, T_c and T_m are reported in Table 1.

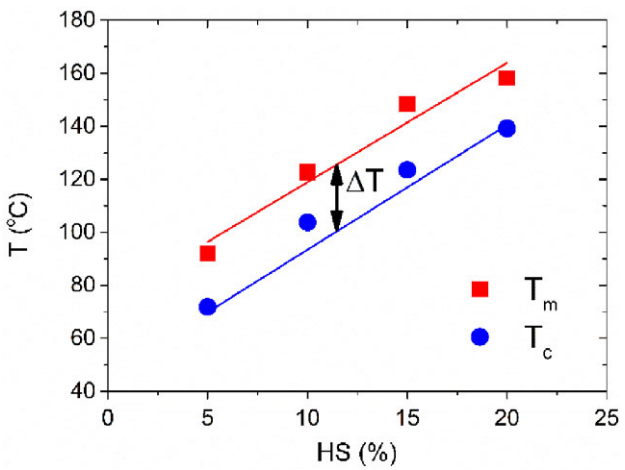

Figure 3. Melting (T_m) and crystallization (T_c) temperatures extracted from conventional DSC performed at 10 °C min^{-1} as a function of HS content.

We present in Fig. 3 the variation of both T_m and T_c with HS content showing that the difference between these two characteristic temperatures ($\Delta T = T_m - T_c$) is rather small (*ca* 20 °C) in comparison with other TPEs such as PBT/pTHF (*ca* 36 °C).[34] This observation suggests a fast crystallization process, most probably due to the presence of strong hydrogen bonds acting over a longer range with respect to their van der Waals analogs, further enhanced by the monomeric (i.e. short and monodisperse) nature of the HSs.[17] Beyond the usual increase of thermal stability (higher T_m) with larger crystallites, conventional DSC also reveals that the melting behavior is rather broad showing multiple melting areas for samples containing more than 5% HSs. Indeed, it seems that well-defined ribbons (melting at the highest T_m) are systematically accompanied by smaller imperfect domains for which the characteristic melting temperature is significantly lower, leading towards broad transition melting. As mentioned in our previous study,[17] we believe that this second population, which corresponds to 'weaker' crystallites, is formed by HSs belonging to chain segments trapped between the most perfect crystallites, i.e. having limited mobility, preventing the formation of more stable structures. In good agreement with the latter statement, this

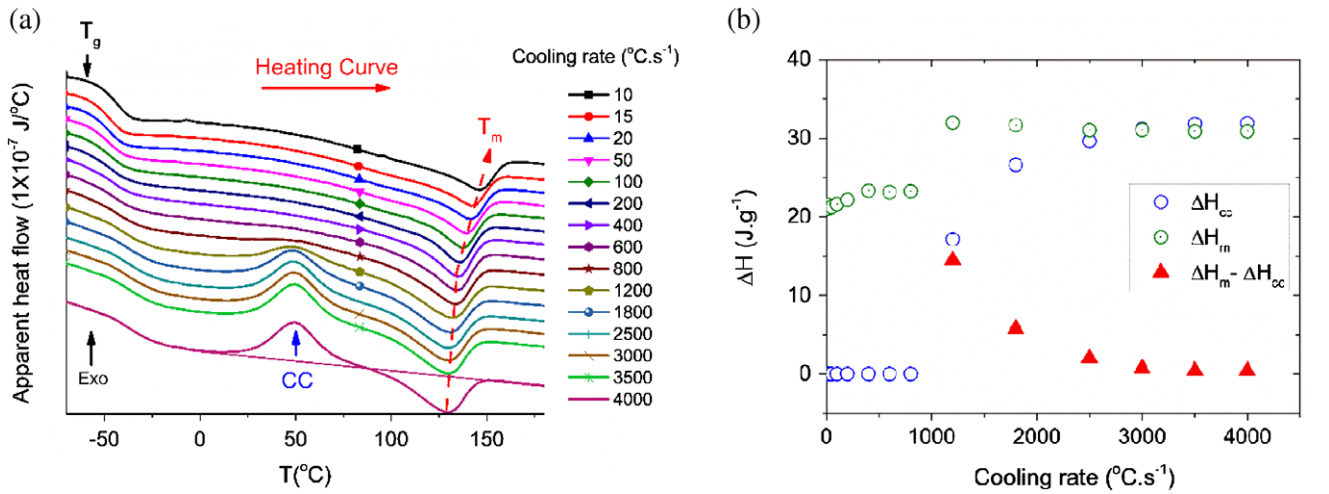

Figure 4. (a) Thermograms measured on a 20% HS sample during a heating step performed at 1000 °C s^{-1}. Prior to the measurements, the sample was cooled from 200 to −80 °C at different cooling rates from 10 °C s^{-1} to 4000 °C s^{-1}. Data are shifted vertically for clarity and the last thermogram shows the flat base line selected for peak integration. (b) Variation of enthalpy in 20% HSs for cold crystallization (ΔH_{cc}), terminal melting (ΔH_m) and the difference ($\Delta H_m - \Delta H_{cc}$) emphasizing the maximum cooling rate (800 °C s^{-1}) at which no crystallization takes place during the cooling phase.

effect greatly disappears when solvent casting is used to prepare TPE films, leading towards a sharp single melting behavior[17] confirming that the sample processing plays a major role in the final sample structure and eventually properties. Conventional thermal analysis does not allow to understand the effect of processing on the final thermal properties and morphology to be thoroughly investigated. The aim of the following FSC experiments is therefore to clarify both kinetic and thermodynamic aspects of such association/dissociation mechanisms and their consequences on the melting properties, through a systematic and progressive variation of the thermal history.

Impact of the cooling rate on the crystallization and melting

The TPE containing 20% HSs was investigated by using the method summarized in Fig. 1(a), with the aim of understanding the effect of high and low cooling rates on the structural evolution of the T4T hard domains. The results are presented in Fig. 4(a) as heating curves recorded at 1000 °C s^{-1} after a cooling step performed at rates from 10 to 4000 °C s^{-1} down to −80 °C. At low temperatures, the thermograms show the glass transition of the pTHF SSs (T_g) around −50 °C, in reasonably good agreement with conventional DSC (see Fig. 2). No clear melting of the SSs can be observed, which suggests that fast cooling prevents SSs from crystallizing. No further attention towards the melting of SSs is taken into account in this paper. Upon increasing the cooling rates above 800 °C s^{-1}, a cold crystallization (CC) peak appears around 50 °C, pointing at the so-called critical or quenching rate.[30] Apparently the T4T HSs stay completely amorphous at cooling rates of 1000 °C s^{-1} or more (see also the AFM results in Fig. 5(a)).[21] For $T > 120$ °C, an endothermal event is seen, undoubtedly indicating the melting of T4T crystallites. In all cases the melting temperature of HSs (shown in Fig. 4(a)) increases in a monotonic way (from 130 to 147 °C) with decreasing cooling rate. The slower the cooling rate is, the better the T4T crystals can organize into well-organized ribbon structures (see also supporting information, Section A.5 and Fig. S4).

In order to evaluate the CC and melting behavior of the HSs, the specific enthalpy variations (±2 J g^{-1}) ΔH_m and ΔH_{cc} were quantified; they are shown in Fig. 4(b)). No CC is observed at low cooling rate, i.e. from 10 °C s^{-1} to 800 °C s^{-1}, providing an almost unchanged $\Delta H_m \approx 22$ J g^{-1} ($X_c \approx 15$ wt%). However, CC starts to occur and ΔH_{cc} significantly increases at rates above 800 °C s^{-1} until it reaches its maximum value of 32 J g^{-1} at quenching rates of 3000 °C s^{-1} and above. On the other hand, the enthalpy of melting at cooling rates below 800 °C s^{-1} is explained by trapping of the T4T HSs due to the ribbons formed during cooling. At fast cooling the formation of these ribbons is more prohibited, which leads, after CC, to an intrinsically higher crystallinity (*ca* 20%). Nevertheless the T_m is slightly lower because CC takes place at 50 °C, which is too low to allow the formation of perfect ribbons as observed upon slower cooling. This suggests that a higher fraction of HSs is able to crystallize during the heating step (by CC) when crystallization is prevented during the cooling step. This result can be understood from the fact that, upon heating, the free HSs will tend to crystallize driven by a very strong attractive potential (due to the low temperature). However, because of a lack of mobility, the so-formed crystallites (appearing at T_{cc}) are expected to be smaller than the crystallites formed below T_c during the cooling phase (see Fig. 5(b)). In good agreement with the latter interpretation, it is found that T_m significantly decreases when CC occurs (see Fig. 4(a)) corroborating the idea that CC leads to a higher fraction of crystallites but limits their size.

Continuous cooling *versus* two-step quenching

We wish to understand the impact of the cooling history on the thermal behavior of the TPE structure from a qualitative variation of the procedure. To do so, we propose to compare the results from the last section (continuous cooling) with so-called 'two-step quenched' materials for which the thermal history is summarized in Fig. 1(b). In the latter case, a critical quenching rate of 4000 °C s^{-1} was used to avoid any crystallization occurring during the successive cooling phases. Between the two quenching steps, and by opposition with continuous cooling, the sample was crystallized isothermally at $T_{iso} = 100$ °C. This temperature was chosen to optimize the crystallization rate (see the section 'Impact of the HS fraction in the chain') while the corresponding time was varied from $t_{iso} = 2$ to $t_{iso} = 60$ s.

For continuous cooling, it is expected that nucleation takes place below T_m, at a certain undercooling grade, and is followed by

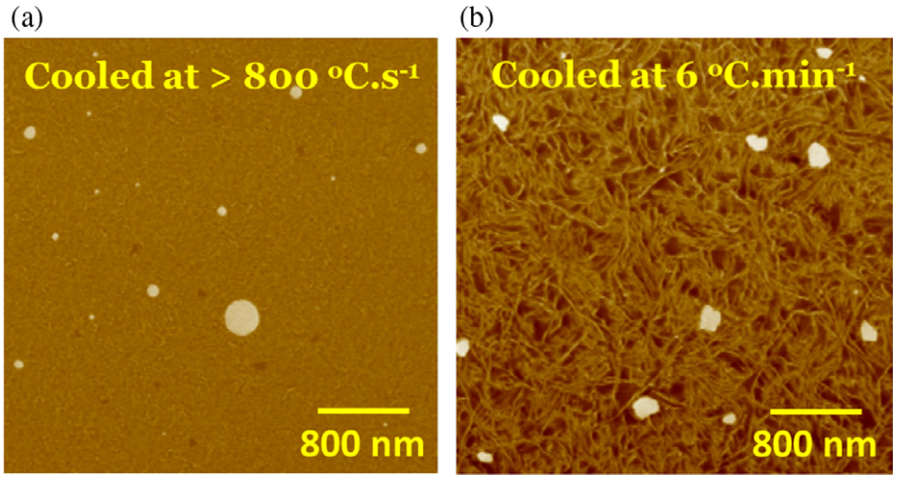

Figure 5. AFM phase image of a 20% HS sample (a) cooled in liquid nitrogen, showing amorphous morphology, and (b) cooled at 6 °C min^{-1} from the melt state (200 °C), showing ribbon structure.

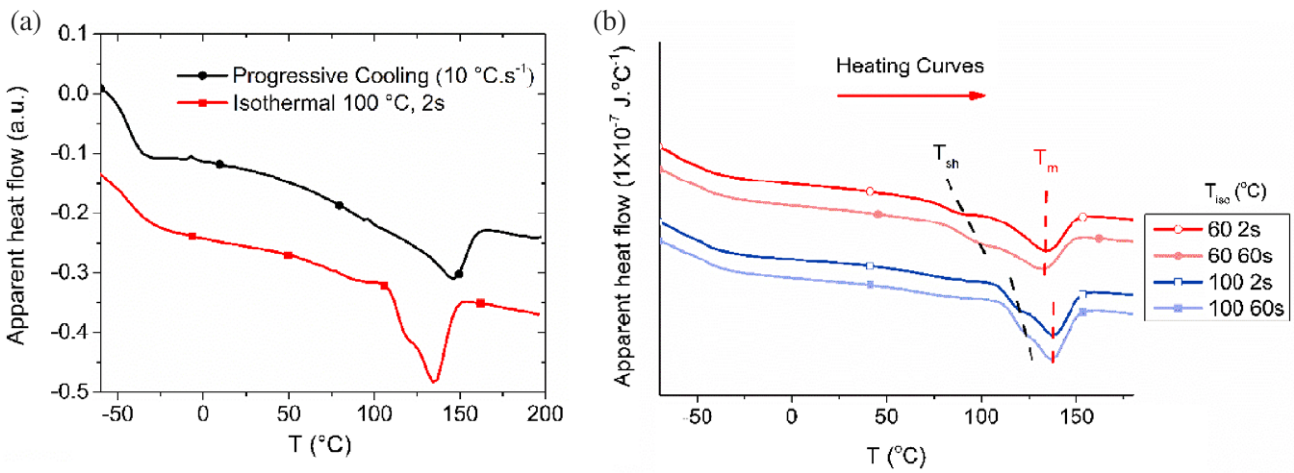

Figure 6. (a) Effect of the cooling procedure: thermograms recorded during the heating phase at 1000 °C s^{-1} on samples progressively cooled at 10 °C s^{-1} from the melt and two-step quenched (4000 °C s^{-1}) maintained for 2 s at 100 °C. Data are shifted vertically for clarity. (b) Thermograms recorded from the 20% HS sample during the heating phase at 1000 °C s^{-1}, after a two-step quenching with T_{iso} = 60 °C and 100 °C. For each sequence, the sample was isothermally held for 2 s and 60 s at T_{iso}. Data are shifted vertically for clarity.

progressive growth of the T4T crystallites, most probably leading to large and stable crystals accompanied by a wide variety of smaller ones. This scenario is corroborated by AFM in Fig. 5(b), where long ribbon-like crystals are clearly observable. As a result, the corresponding melting peak in Fig. 6(a) is rather broad, confirming the large polydispersity in crystal size. On the other hand, when two-step quenching is applied, the TPE quickly crystallizes due to the high (thermodynamic) association rate at T_{iso} = 100 °C, therefore strongly limiting the 'progressive' character of the ribbon growth. In fact, this procedure results in a lower melting temperature and a sharper melting peak made of two distinct contributions denoted T_m and T_{sh} (see Fig. 6(a)). This bimodal distribution is due to a primary crystallization at early stages, i.e. when the copolymers still have a high mobility, followed by a secondary crystallization (related to T_{sh}) due to the association of chain segments having their extremities trapped into the primary network.[17] Because of their reduced mobility, these HSs take time to crystallize and the corresponding growing crystals cannot reach their equilibrium size if t_{iso} is too short. This picture is further validated in Fig. 6(b), where it is seen that the second melting peak (T_{sh}) is more visible when t_{iso} is shorter, i.e. when the waiting time does not allow the crystallites to fully grow. In contrast, if a longer t_{iso} is used (60 s instead of 2 s), this secondary peak is shifted towards higher melting temperatures and eventually merges with the main melting peak (T_m). In addition, Fig. 6(b) shows that decreasing T_{iso} from 100 to 60 °C results in lower temperatures for T_m and T_{sh} respectively. Considering the slower crystallization rate at 60 °C (see the section 'Impact of the HS fraction in the chain'), synonymous with a lower chain mobility, we believe that the secondary crystals formed at 60 °C are far from their equilibrium state, in comparison with the crystals created at 100 °C, explaining the large difference in T_{sh}. We also observe that the fraction of equilibrated ribbons is smaller, with a more pronounced size dispersion than at T_{iso} = 100 °C. The impact of both T_{iso} and t_{iso} are investigated systematically in the next two sections.

Impact of T_{iso} on the TPE crystallization

In order to further understand the thermal behavior of these copolymers, we propose in this section to vary T_{iso} from T_m to T_g

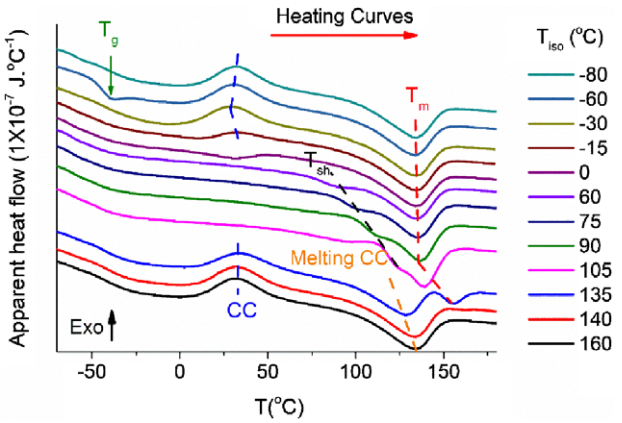

Figure 7. Thermograms recorded from the 20% HS sample during the heating phase at 1000 °C s^{-1}, after a two-step quenching with varying T_{iso} from T_m to T_g. For each sequence, the sample was isothermally held for 2 s at T_{iso}. Data are shifted vertically for clarity.

and to investigate the influence on crystallite formation following the procedure depicted in Fig. 1(b). Representative thermograms are presented in Fig. 7, showing a rich variety of melting behaviors that we analyze below by separating the isothermal temperatures into several regions. (The whole data set without vertical shift factor can be found in supporting information, Section A.6)

For $T_{iso} \geq 140$ °C, the thermograms are similar to those extracted from direct rapid quenching (Fig. 4). This is in good agreement with the fact that the material stays amorphous after 2 s spent at these high values of T_{iso}. It is subsequently quenched below its T_g, giving no chance for crystallization to occur during the cooling phase. Therefore, once the material is heated back, one expects CC (seen at around 35 °C) followed by the melting of the so-formed crystallites (seen at around 135 °C). A difference with the continuous cooling procedure can be noticed, however, in the temperature at which CC occurs. In fact, it is found to be *ca* 15 °C below the temperature reported in Fig. 4. This difference is attributed to the formation of pre-nuclei formed during the 2 s isothermal break (since $T_{iso} < T_m$) due to intramolecular and intermolecular hydrogen bond association in the melt, implying a deepening of phase separation which is likely to enable CC to occur earlier during the subsequent heating.[35]

At $T_{iso} = 135$ °C an additional peak appears at high temperature (*ca* 155 °C) suggesting the creation of very stable crystallites, whereas this is not observed any more for lower T_{iso}. We assign this melting peak to the fact that, at such high T_{iso}, the chains have a large mobility which gives them time to disentangle and diffuse (similarly to solvent casting) before starting to crystallize, thus favoring the creation of well-organized crystals within the isothermal time frame. The melting peak at high temperatures resides of annealing at 135 °C which is within the melting area of the T4T crystals shown in Fig. 7. On the other hand, it is observed that not all T4T crystals crystallize into such strong crystals, the remaining HSs cold crystallizing during the heating process. The latter is attributed to the low driving force for crystallization at high T_{iso}. In conclusion, crystallization just below T_c seems of particular interest since it allows crystallite formation from chains having an optimal mobility.

By decreasing T_{iso} further, from **135 °C to 105 °C**, this equilibrium between chain mobility and crystallization driving force is modified toward a higher crystallization rate (see the section 'Impact of the HS fraction in the chain') and lower chain mobility. In particular, it is observed that the lower T_{iso} is, the lower is T_m but the higher is the melting enthalpy. This can be attributed to the fact that a higher crystallization rate leads to the formation of a larger number of smaller crystallites, which cannot grow further due to the lower mobility of the (associated) chains. Also, while some of the HSs are seen to crystallize during the cooling phase, a significant fraction of them is observed to cold crystallize during the subsequent heating (Section A.6, Fig. S5(a)). The corresponding CC temperature is found to be higher than that reported for higher T_{iso}, strongly suggesting that the HS associations made along the cooling step hinder the chains' motion. This is also supported by a lower melting point of the smaller crystals originating during CC.

For 0 °C < T_{iso} < 105 °C, CC is no longer observed since the sample has a high crystallization rate and fully crystallizes during the isothermal 2 s break. Completing the preceding results, Fig. 7 further reveals that the melting temperature T_m of the largest ribbons formed in this range of temperatures is nearly independent of T_{iso}. More precisely, as observed in Figs S5(b) and S5(c), decreasing T_{iso} from 105 °C to 50 °C leads to the formation of a few crystallites melting at lower temperatures, while decreasing T_{iso} from 50 °C to 0 °C does not influence the melting behavior of the crystallites any more. In both cases, T_m is much lower than the high melting temperature observed at $T_{iso} = 135$ °C. It must be noted here that this high melting peak cannot be attributed to a melting recrystallization process as observed in several semicrystalline polymers. Indeed, one can disprove this possibility since the melting temperature of the high melting peak is not affected by varying the heating rate. This suggests that in this range of temperature crystal formation is mostly governed by the high thermodynamic driving force, leading to fast formation of ribbons taking place before any significant chain diffusion and allowing the eventual creation of strong crystallites (high T_m).

In contrast, the melting temperature T_{sh} of the secondary peak decreases in a monotonic way with decreasing T_{iso} until disappearing when the latter reaches 0 °C. As already suggested, this secondary melting peak can be attributed to the melting of short metastable crystallites (called here 'baby-ribbons'). Based on these results as well as Figs S5(b) and S5(c), it can be postulated that the melting temperature T_{sh} is related to their size, i.e. decreasing T_{iso} would make them smaller and smaller. This scenario is further supported by the fact that, at a temperature at which the shoulder peak disappears ($T_{iso} = 0$ °C), part of the HSs have too low a mobility even to be able to create short crystals during the 2 s break at T_{iso} and CC appears again ($T_{iso} = -15$ °C). The decreasing size of these baby-ribbons with decreasing T_{iso} is a direct consequence of the very low mobility of the chain segments, as further discussed in the section 'Impact of the HS fraction in the chain'.

Finally, **for $T_{iso} < 0$ °C** the experiments in Fig. 7 are similar to that in Fig. 4 since the sample is quenched from 200 °C to a temperature close to T_g at which no significant crystals have time to develop due to the quasi-arrested chain dynamics. Around T_g the growth of the T4T crystals is highly restricted due to very low chain mobility. This is also shown by a decreasing crystallization rate, observed when reaching 0 °C (see the section 'Impact of the HS fraction in the chain'). As already mentioned, at $T_g = -15$ °C, CC reappears at the same temperature as previously observed (*ca* 35 °C).

Influence of holding time t_{iso}

General trend

In Fig. 7, the 2 s waiting time at T_{iso} is not long enough to reach a thermodynamic equilibrium (e.g. CC is detected for high and low T_{iso} values). Therefore, the waiting time was increased to

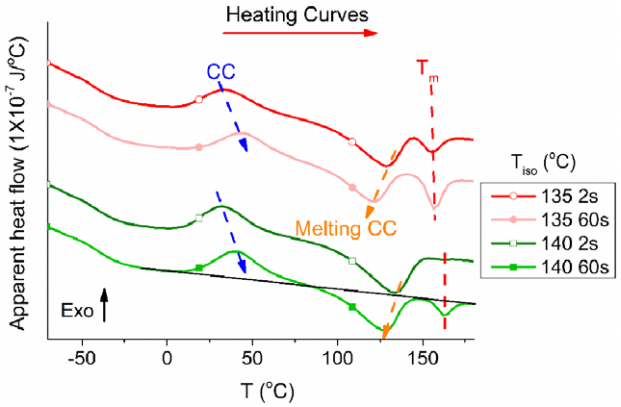

Figure 8. Thermograms recorded during the heating phase (1000 °C s^{-1}) of the 20% HS sample after a two-step quenching (4000 °C s^{-1}) with t_{iso} being either 2 or 60 s and T_{iso} = 135 or 140 °C. Data are shifted vertically for clarity and the selected base line for integrating the peaks is shown.

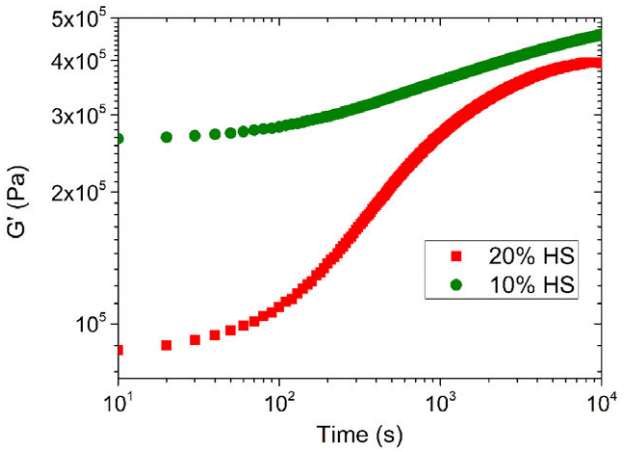

Figure 9. Storage modulus (G') at 10 rad s^{-1} as a function of holding time (s) for an isothermal temperature $T_{exp} = T_c + 10$ °C.

t_{iso} = 60 s (see Fig. 8) in order to understand the development of the ribbon-like structure. First, it is seen that at T_{iso} = 135 °C and 140 °C a longer waiting time allows the fraction of much more perfect crystallites to be enhanced, characterized by a very high melting temperature. This phenomenon, which is called annealing, can be quantified by looking at the enthalpy variation of the end melting which grows significantly in both cases (see Table 2). One hypothesis is that there is a lamellar doubling of the ribbon-like crystals. This may explain the discontinuity observed in the melting and the high end melting temperatures. This result is in line with the discussion proposed in the previous section: a high value of T_{iso} (around T_c) leads to much more perfectly organized crystals, taking, however, a long time to grow due to their low crystallization driving force. Furthermore, it appears unambiguously that a longer t_{iso} pushes up the temperature of CC. This observation can be simply rationalized through similar arguments to those previously mentioned, i.e. increasing t_{iso} (or decreasing T_{iso}) favors chain association, which limits the segment mobility when heating and therefore delays CC.

A full quantitative analysis of various enthalpies observed such as cold crystals (ΔH_{cc}), the melting of cold crystals (ΔH_{mcc}) and end melting (ΔH_m) was extracted using a suitable baseline and is shown in Fig. 8, supporting our qualitative conclusions (see Table 2). The increase of T_m with t_{iso} is due to the annealing effect, as a longer waiting time allows a better stacking of hydrogen-bonded HSs. It can also be noted that the enthalpies of CC (ΔH_{cc}) and the associated melting (ΔH_{mcc}) are very close to each other, avoiding any doubt about the nature of such phase transitions. Furthermore, around T_c, increasing the isothermal temperature provides the chance to form a more perfect crystal structure (higher T_m) despite the longer time needed to develop it (lower ΔH_m). The latter point suggests once again that a higher mobility of the chains leads to the formation of larger objects (as is the case in solvent cast TPEs), characterized by higher melting temperatures. There is thus always a balance between ribbon crystals and the baby-ribbon crystallite structures.

The previous explanation and observations are further confirmed by the rheology measurements presented in Fig. 9. It shows the evolution of the storage modulus for multi-block copolymers containing 10% and 20% HSs as a function of time, measured under small oscillatory shear measurements performed at a frequency of 10 rad s^{-1}. The temperature T_{exp} of the experiment was reached at 6 °C min^{-1} from 200 °C. It was chosen such that $T_{exp} = T_c + 10$ °C, i.e. 113 °C for 10% HSs and 150 °C for 20% HSs.

Despite the temperature being above T_c, the storage modulus continuously increases with time, which suggests that the HSs associate more and more to form new or larger crystals. Crystallization is thus possible at such high temperature but at a very low crystallization rate. As seen in Fig. 9, the corresponding modulus continuously increases during a very long period of time and only starts to saturate after around 10^4 s, indicating that the systems are slowly approaching their equilibrium state. Thus, based on these results, it can be concluded that in the temperature range at which the crystallization rate is slow a longer waiting time t_{iso} at isothermal temperature favors the creation of a larger fraction of crystallites. As a last comment on Fig. 9, it must be noted that the fact that the initial modulus of the 10% HS sample is larger than that measured for the 20% HS sample is due to the difference in the temperature of measurement (113 °C *versus* 150 °C).

In order to extend these observations to the full range of T_{iso} we summarize in Fig. 10 the evolution of the end melting point (T_m) and the corresponding melting temperature of the secondary peak (T_{sh}) as a function of T_{iso} for 2 s and 60 s. It should be remembered that these experiments still refer to the two-step quenching

Table 2. Variation of enthalpies in 20% HS samples for cold crystallization (ΔH_{cc}), the melting of cold crystals (ΔH_{mcc}) and the terminal melting point (ΔH_m)

T_{iso} (°C)	Isothermal time (s)	T_{cc} (°C)	ΔH_{cc} (J g^{-1})	T_{mcc} (°C)	ΔH_{mcc} (J g^{-1})	T_m (°C)	ΔH_m (J g^{-1})	X_c (%)
140	2	32	34.8	134	34.4	–	–	–
	60	40	28.6	128	30.9	163	4.4	2.9
135	2	33	28.4	129	31.5	156	7.0	4.6
	60	42	24.2	121	26.1	156	10.6	7.0

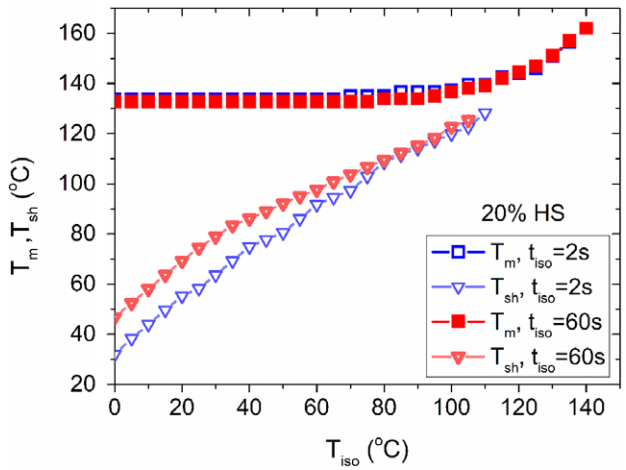

Figure 10. Terminal melting temperature of the crystallites (T_m) and the melting temperature of the secondary peak (T_{sh}) as a function of isothermal temperature (T_{iso}) for a waiting time t_{iso} of 2 s and 60 s.

procedure (4000 °C s^{-1}) on a TPE containing 20% HSs. This representation means that several important features can be highlighted: (i) the end melting point of the T4T crystallites is nearly constant (*ca* 135 °C) for 0 °C < T_{iso} < 100 °C whereas, beyond this point, it continuously increases up to 160 °C at T_{iso} = 140 °C (*ca* T_c in conventional DSC); (ii) the melting temperature of the secondary peak evolves in a quasi-linear way with T_{iso}; and (iii) while the waiting time at T_{iso} has no effect on T_m (whatever the value of T_{iso}), it significantly enhances T_{sh} by *ca* 15 °C for T_{iso} < 80 °C.

These results are consistent with our hypothesis that the secondary melting point T_{sh} is associated with the melting of shorter crystal structures, defined as baby-ribbons, which did not have time to grow to their final, equilibrium state.

Furthermore, observations (i) and (iii) are understood as from T_{iso} = 0 to 100 °C the crystallites had time to grow and to reach their thermodynamic equilibrium, which leads to similar crystals in all this range of T_{iso}. Indeed, in this range of temperatures, a longer waiting time between the two temperature ramps does not affect the final melting point T_m. Moreover, as discussed with regard to Fig. 7, the crystallization rate of the HSs is too fast compared to the necessary time for the whole chain to diffuse and better organize, so the formation of a much more perfect crystal (with T_m above 140 °C) is prevented. Therefore, the equilibrium state of such a crystal corresponds to the best crystallites which can be built, knowing that the driving force for crystallization is high and that the HSs can only diffuse locally. This leads to crystallites with a moderately high melting point.

Above this temperature, the large mobility of the chains ($T = T_g$ + 160 °C) allows them to disentangle and diffuse in a larger length scale, and the crystallites are characterized by a higher melting point (i.e. the one visible in conventional DSC, Fig. 2, due to the low cooling rate), but they are only present in a small proportion (see the previous section). It is also observed that waiting a longer time at T_{iso} does not influence their melting point, while the proportion of crystals increases (see Fig. 8).

Observation (ii), already commented on above, highlights an important point. Whilst it is clear that 2 s is enough for stable crystallites to form in a broad range of T_{iso}, the reduction of the mobility caused by the latter and by the low temperature limits the subsequent formation of metastable baby-ribbons, explaining the drop in T_{sh}.

Observation (iii) confirms that the baby-ribbons associated with the secondary melting peak are non-equilibrated structures. Indeed, the higher melting point measured for a longer time at T_{iso} confirms their growing nature, possibly leading subsequently to a merging with a larger crystallite.

Impact of the HS fraction in the chain

Here, we propose to investigate a parameter playing a crucial role in the crystallite structure: the HS content, i.e. the number of T4T groups along the TPE chains. As already shown from small-angle X-ray scattering and rheology measurements,[17,36] this parameter is responsible for a drastic change in the crystallite size, which should strongly impact the thermomechanical properties (e.g. modulus and melting point) of the samples.

In Fig. 11, we investigate the influence of HS content on the evolution of the melting temperatures T_m and T_{sh}. Figure 11(a) reveals that while the melting point (T_m) is lower for the 10% HS sample than for the 20% HS sample due to the formation of smaller stable crystallites,[37] the melting temperature T_{sh} associated with the baby-ribbons remains unchanged. This observation suggests that similar metastable crystals are created in both samples, their growth being limited by the same mechanisms, related to the local dynamics of the molecular segments (trapped between two associated HSs) and the ability of the free HSs to explore their surroundings. In both samples, it is observed that longer waiting times lead to higher values of T_{sh}, as already discussed.

When t_{iso} is increased from 2 s to 60 s (see Fig. 11(b)), a significant increase of the melting point (T_m) from 113 till 139 °C is observed for the 10% HS sample, while it stays constant for the 20% HS sample. This means that the crystallization rate of the 10% HS sample is too slow to allow the T4T crystallites to reach their critical size (or thermodynamic equilibrium) after 2 s. Thus, the formation of larger and stronger ribbons requires a longer waiting time t_{iso}. In contrast, for the 20% HS sample, the crystallites formed during the isothermal break have time to reach their critical size after 2 s and will not grow further by waiting 60 s (see Fig. 11 and related discussion Section 3.5 i.e. impact of the HS fraction in the chain).

As already observed with the 20% HS sample, high melting temperatures T_m can be obtained if the sample is brought to isothermal temperatures just below T_c (=104 °C for 10% HS via conventional DSC, see Table 1), the temperature at which the chains have time to diffuse before starting to crystallize. However, since the crystallization rate of the 10% HS sample is significantly lower than that of the 20% HS sample, such crystals do not have time to be formed if the break at T_{iso} is too short (see Fig. 11(a), with a 2 s break), and only CC crystals are observed. Therefore, a longer waiting time must be considered (such as 60 s, see Fig. 11(b)) in order to allow these very stable crystals to grow.

Therefore, the melting temperatures corresponding to T_{iso} between 40 °C and 60 °C are not reported in Fig. 11(b). Indeed, in this range of temperature, both the melting peak and the secondary melting peak are merging and one cannot easily determine their respective temperatures (see supporting information, Section A.7 and Fig. S6).

In order to summarize the above observations, we compare in Fig. 12 the crystallization rates of the 10% HS and 20% HS samples, as a function of their isothermal temperature. The crystallization rates have been extracted according to the method developed by Vander Poel[30] (also see supporting information, Sections A.8 and A.9, Figs. S7 and S8). For the 20% HS sample, a bimodal distribution of crystallization rate is observed, with two maxima located at

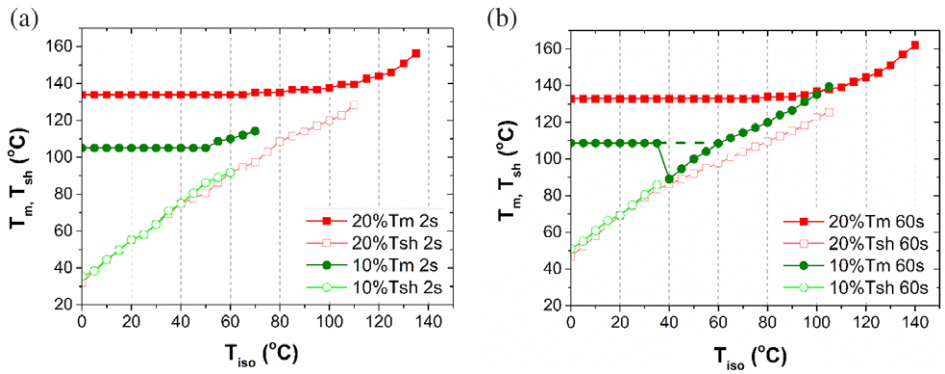

Figure 11. Melting temperature (T_m) and secondary peak melting temperature (T_{sh}) for 10% and 20% HS TPE as a function of isothermal temperature for a waiting time of 2 s (a) and 60 s (b).

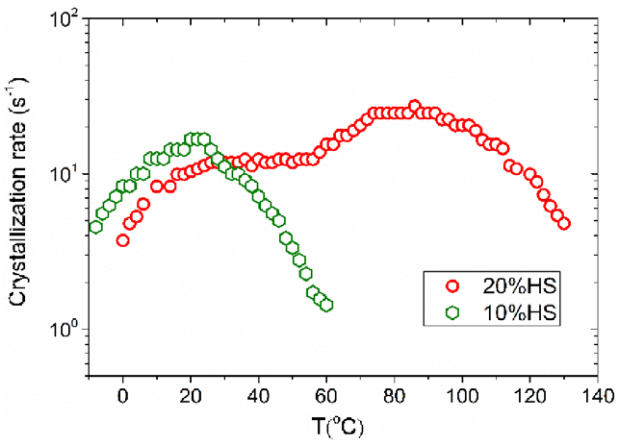

Figure 12. Crystallization rate as a function of temperature T_{iso} for 10% and 20% HS samples.

86 °C and 36 °C, while the 10% HS sample only shows one maximum, located at around 25 °C. These maxima are unambiguously related to the crystallization of the T4T units, arising from the balance between the thermodynamically driven crystallization forces and the chain mobility. In the case of the 20% HS sample, the maximum located at high T can easily be explained based on the discussion in the previous two sections. Starting from high T_{iso}, as expected from the Turnbull–Fisher description,[24] the crystallization rate increases as the thermodynamic driving force for nucleation increases due to supercooling of the sample.[38] Consequently, as long as thermodynamic forces dominate, the crystallites grow faster and faster with decreasing T_{iso}. However, decreasing T_{iso} further, the thermodynamic effect is counterbalanced by the reduced intrinsic chain mobility, which slows down crystal formation.[39] Therefore, because of these two mechanisms, there is an optimum temperature, 86 °C, at which the crystallization rate is maximum. Below this maximum temperature, weaker crystals are formed, all characterized by a similar melting temperature (see Fig. 11(a)), and a significant reduction of the crystallite formation rate is observed.

Then, at around 55 °C, the crystallization rate of the 20% HS sample stops decreasing and reaches a quasi-plateau before falling again at 20 °C, generating the second maximum. While its origin is not fully clear, such a bimodal distribution was already observed for PBT and other polymers in the literature.[30] It was attributed by Pyda *et al.*[40] to the possible formation of an amorphous–rigid fraction or to change of the crystal structure and dimensions.[39,41–43] In the present case, we propose the following picture to explain this behavior. At around T_{iso} = 55 °C, the large-scale diffusion of the chains is becoming so slow that it does not take place any more. However, locally, the molecular segments (e.g. trapped between two consecutive entanglements or two associated HSs) still have a large mobility and can easily explore their (close) surroundings and crystallize into a less perfect crystal structure, i.e. baby-ribbon. Therefore, combined with a high driving force for crystallization, the corresponding rate is constant as long as local mobility is not affected by temperature, and the ribbons obtained are all characterized by exactly the same melting peak and melting temperature T_m (see Fig. S5(c)). Moreover, a decrease of the crystallization rate is then observed below 20 °C, when local mobility of the entangled segments starts to be affected, and it disappears at T_{iso} < 0 °C, reaching its T_g value. Basically one can depict the bimodal clock-curve as a sum of two separate clock-curves: one for the ribbon-like crystals, and the other for imperfect crystals due to decreased chain mobility. If we refer to the work of Androsch *et al.*,[44] these different types of crystal could be attributed to a change in the nucleation mechanism, depending on the chain mobility.

On the other hand, in the case of the 10% HS sample, only one maximum is observed in the crystallization rate curve. This is attributed to its much lower melting temperature: above 60 °C, thermodynamic forces for crystallization are too slow to compete with chain mobility. The crystallization rate only increases at lower temperature, when chain diffusion is becoming slow enough. So, in the case of the 10% HS sample only one type of ribbon-like crystal can be formed. In order to prove this concept, real time flash combined with X-rays should be performed.[46]

To conclude, according to the proposed picture, a bimodal distribution of the crystallization rates can be observed if both the temperature at which crystallization starts and the temperature at which global diffusion of the chains is suppressed (due to chain entanglements or chain segments trapped between associated HSs) are much higher than the temperature at which the segmental dynamics are slowed down. Since the mobility of the chains strongly depends on their length and on the average number of HSs they contain, we expect that the position of the high temperature peak could be varied with sample composition, which will be tested in future work.

CONCLUSIONS

To summarize, by using FSC, we have shown in this work the great variety of phases likely to exist in well-defined TPEs. In particular,

by exploring different thermal manipulations, we demonstrated that different structures, i.e. different properties, were reachable, being potentially of a great interest for industry. In particular, we showed on one side that a progressive cooling step was allowing the crystallites to grow in a rather homogeneous way from nucleation points, whereas on the other side a sudden quenching between T_m and T_g was leading to amorphous HSs or a high fraction of smaller and metastable baby-ribbons depending on the isothermal temperature. While in the former case stronger mechanical properties are expected, the latter is more likely to provide the material's higher electrical permittivity confirming the great polyvalence of such polymers in terms of applications (fibers, electrolytes etc.). From a more fundamental point of view, we were able to accurately quantify the minimal cooling rate that allows the TPE 20% HSs to be kept amorphous when quenched from the melt state at −800 °C s^{-1}. This extreme value appears as a strong asset for this particular chemistry since it allows hard network formation and thus the material elasticity to emerge in a quasi-instantaneous way. We also showed how playing with the temperature for these TPEs allows the influence of chain mobility to be controlled, both at the level of the whole chains and at a more local level in the formation of stable ribbons.

Finally we believe that the great opportunity of this experimental methodology is to be able to distinguish and isolate the phases that are involved in the main thermal transitions. This information, coupled with the characterization of mechanical properties, is a crucial step towards a deeper understanding of the structure–property relationship in these TPEs.

ACKNOWLEDGEMENTS

This work has received funding from the People Programme (Marie Curie Actions) of the European Union's Seventh Framework Programme (FP7/2007-2013) under REA grant agreement no. 607937. We would like to thank Pascal Van Velthem for helping with the FSC instrument and Dr Shashi Poddar for AFM measurements at the Université Catholique de Louvain, Louvain-la-Neuve, Belgium. EVR thanks the FNRS (as 'chercheur qualifié').

CONFLICT OF INTEREST

The authors declare no competing financial interest.

SUPPORTING INFORMATION

Supporting information may be found in the online version of this article.

REFERENCES

1 Holden G, Legge NR, Quirk RP and Schroeder HE, *Thermoplastic Elastomers*. Hanser Publisher, Munich (1996).
2 Serrano PJM, van de Werff BA and Gaymans RJ, *Polymer* **39**:83–92 (1998).
3 Leibler L, *Macromolecules* **13**:1602–1617 (1980).
4 Vinogradov G, Dreval V, Malkin AY, Yanovsky YG, Barancheeva V, Borisenkova E *et al.*, *Rheol Acta* **17**:258–263 (1978).
5 Eisenbach CD, Baumgartner M and Günter C, Polyurethane elastomers with monodisperse segments and their model precursors: synthesis and properties, in *Advances in Elastomers and Rubber Elasticity*, ed. by Lal J and Mark JE. Springer US, Boston, MA, pp. 51–87 (1986).
6 Stribeck N, Fakirov S, Apostolov AA, Denchev Z and Gehrke R, *Macromol Chem Phys* **204**:1000–1013 (2003).
7 Gabriëlse W, Soliman M and Dijkstra K, *Macromolecules* **34**:1685–1693 (2001).
8 van der Schuur M and Gaymans RJ, *J Polym Sci A Polym Chem* **44**:4769–4781 (2006).
9 Niesten MCEJ, Feijen J and Gaymans RJ, *Polymer* **41**:8487–8500 (2000).
10 Van Hutten P, Mangnus R and Gaymans R, *Polymer* **34**:4193–4202 (1993).
11 Chapman AV and Porter M, Sulphur vulcanization chemistry, in *Natural Rubber Science and Technology*, ed. by Roberts AD. Oxford University Press, New York, NY, p. 516 (1988).
12 Arun A, Dullaert K and Gaymans RJ, *Polym Eng Sci* **50**:756–761 (2010).
13 Appel WPJ, Portale G, Wisse E, Dankers PYW and Meijer EW, *Macromolecules* **44**:6776–6784 (2011).
14 Miller JA, Lin SB, Hwang KKS, Wu KS, Gibson PE and Cooper SL, *Macromolecules* **18**:32–44 (1985).
15 Gaymans R and De Haan J, *Polymer* **34**:4360–4364 (1993).
16 Biemond GJE, Feijen J and Gaymans RJ, *J Appl Polym Sci* **105**:951–963 (2007).
17 Baeza GP, Sharma A, Louhichi A, Imperiali L, Appel WPJ, Fitié CFC *et al.*, *Polymer* **107**:89–101 (2016).
18 Odarchenko YI, Anokhin DV, Doblas D, Rosenthal M, Hernandez JJ, Vidal L *et al.*, *Macromolecules* **47**:7890–7899 (2014).
19 Biemond GJE, Feijen J and Gaymans RJ, *Polym Eng Sci* **48**:1389–1400 (2008).
20 Serrano PJM, Van Bennekom ACM and Gaymans RJ, *Polymer* **39**:5773–5780 (1998).
21 Gaymans RJ, *Prog Polym Sci* **36**:713–748 (2011).
22 Hobbs S and Pratt C, *Polymer* **16**:462–464 (1975).
23 Nichols ME and Robertson RE, *J Polym Sci B* **30**:305–307 (1992).
24 Van Bennekom A and Gaymans R, *Polymer* **38**:657–665 (1997).
25 Aharoni SM, *Macromolecules* **21**:1941–1961 (1988).
26 Schick C and Mathot V eds, *Fast Scanning Calorimetry*, Vol. 1680. Springer, Switzerland (2016).
27 Mathot V, Pyda M, Pijpers T, Vanden Poel G, van de Kerkhof E, van Herwaarden S *et al.*, *Thermochim Acta* **522**:36–45 (2011).
28 Zhuravlev E and Schick C, *Thermochim Acta* **505**:1–13 (2010).
29 Vanden Poel G, Istrate D, Magon A, and Mathot V, *J Therm Anal Calorim* **110**:1533–1546 (2012).
30 Schick C and Mathot V, *Fast Scanning Calorimetry*, Chapter 18. Springer International Publishing Switzerland, pp. 611–632 (2016).
31 Poel GV, Sargsyan A, Mathot V, Assche GV, Wurm A, Schick C *et al.*, *Int J Nanomedicine* **9**:975–984 (2011).
32 Schick C and Mathot V, *Fast Scanning Calorimetry*, Chapter 1. Springer, pp. 3–80 (2016).
33 Chen Y, Chen X, Zhou D, Shen Q-D and Hu W, *Polymer* **84**:319–327 (2016).
34 Niesten MCEJ and Gaymans RJ, *J Appl Polym Sci* **81**:1372–1381 (2001).
35 Zhuravlev E, Schmelzer JWP, Androsch R and Schick C, *Int Polym Proc* **31**:628–637 (2016).
36 Baeza GP, *Macromolecules* **51**:1957–1966 (2018).
37 Flory PJ, *Trans Faraday Soc* **51**:848–857 (1955).
38 McCrum NG, Buckley CP and Bucknall CB, *Principles of Polymer Engineering*. Oxford University Press, USA (1997).
39 Höhne GWH, *Polymer* **43**:4689–4698 (2002).
40 Pyda M, Nowak-Pyda E, Heeg J, Huth H, Minakov AA, di Lorenzo ML *et al.*, *J Polym Sci B* **44**:1364–1377 (2006).
41 Silvestre C, Cimmino S, Duraccio D and Schick C, *Macromol Rapid Commun* **28**:875–881 (2007).
42 Mileva D and Androsch R, *Colloid Polym Sci* **290**:465–471 (2012).
43 Zhuravlev E, Schmelzer JWP, Wunderlich B and Schick C, *Polymer* **52**:1983–1997 (2011).
44 Jariyavidyanont K, Androsch R and Schick C, *Polymer* **124**:274–283 (2017).
45 van Drongelen M, M-V T, C D, P G, P GV and A R, *Thermochim Acta* **563**:33–37 (2013).
46 Baeten D, Mathot VBF, Pijpers TFJ, V. O, P. G, van Puyvelde P *et al.*, *Macromol Rapid Commun* **36**:1184–1191 (2015).

